Electronic Supplementary Information for:

Enhancing Enantioselectivity in Chiral Metal Organic Framework Fluorescent Sensors

Shannon Thoonen[a,b], Pattara Siripanich[a], Lisa Hua[d], Hui Min Tay[a,c], Pria Ramkissoon[a,e], Trevor A. Smith[a,e], Martina Lessio[d], Carol Hua[*a,e]

[a] *School of Chemistry, The University of Melbourne and* [e] *ARC Centre of Excellence in Exciton Science, Parkville, Victoria 3010, Australia;*
[b] *School of Chemistry, Monash University, Clayton, Victoria , Australia;*
[c] *Department of Chemistry, University of Oxford, Oxford OX1 3TA, UK*
[d] *School of Chemistry, University of New South Wales, Kensington, New South Wales 2052, Australia*
Corresponding author e-mail address: carol.hua@unimelb.edu.au

Table of Contents

Synthesis of Ligands

(*S*)-4,4'-Dibromo-2,2'-diethoxyl-1,1'-binapthalene.[1] (*S*)-4,4'-dibromo-2,2'-binapthol (0.370 g, 0.83 mmol), bromoethane (0.371 mL, 5.00 mmol), NaI (0.019 g, 0.13 mmol) and K_2CO_3 (0.576 g, 4.17 mmol) were suspended in acetone and heated at reflux for 18 hours. The reaction mixture was filtered, then the filtrate concentrated under reduced pressure. The oily residue was washed with hexane (2 mL) to give the product as an orange powder (0.35 g, 84%). ^{1}H NMR (400 MHz, $CDCl_3$) δ 8.23 (d, 2H, J = 8.8 Hz), 7.73 (s, 2H), 7.43-7.39 (m, 2H), 7.24-7.22 (m, 2H), 7.10 (d, 2H, J = 8.4 Hz), 4.08-4.00 (m, 4H), 1.07 (t, 6H, J = 6.8 Hz) ppm.

(*S*)-4,4′-(2,2′-diethoxy-[1,1′-binaphthalene]-4,4′-diyl)dipyridine ((*S*)-L_1). A suspension of (*S*)-4,4′-dibromo-2,2′-diethoxy-1,1′-binaphthalene (0.32 g, 0.62 mmol), pyridyl-4-boronic acid (0.23 g, 1.86 mmol), $Pd(PPh_3)_4$ (0.045 g, 0.039 mmol) and K_2CO_3 (0.43 g, 3.10 mmol) in 1,4-dioxane (12.5 mL) and H_2O (1.25 mL) was degassed under N_2 and heated to reflux for 16 hours. The solvent was removed under reduced pressure to give a red residue, which was partitioned between H_2O (30 mL) and CH_2Cl_2 (30 mL). The aqueous layer was extracted with CH_2Cl_2 (2 × 30 mL), then the combined organic layers were dried over $MgSO_4$, filtered and the solvent removed under reduced pressure. The resulting red oil was triturated with ether and dried in air to afford the product as an orange powder (0.31 g, 97%). ^{1}H NMR (400 MHz, $CDCl_3$) δ 8.85 (br s, 4H), 7.86 (d, J = 8.0 Hz, 2H), 7.62 (br s, 4H), 7.39 (s, 2H), 7.37 – 7.15 (m, 6H), 4.23 – 4.00 (m, 4H), 1.14 (t, J = 7.0 Hz, 6H) ppm. ^{13}C{^{1}H} NMR (101 MHz, $CDCl_3$) δ 153.8, 149.9, 148.9, 138.8, 134.7, 126.7, 126.6, 126.1, 125.4, 124.3, 121.0, 116.7, 65.4, 15.1 ppm. HRMS (ESI) m/z: $[M+H^+]^+$ calc'd for $[C_{34}H_{28}N_2O_2]^+$,497.2229; found, 497.2417.

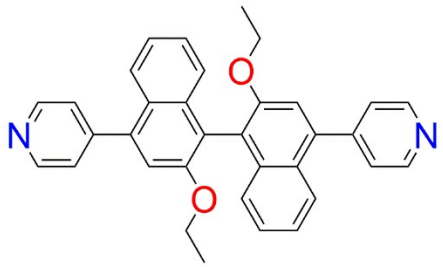

(*S*)-4,4′-(2,2′-dialcohol-[1,1′-binaphthalene]-4,4′-diyl)dipyridine ((*S*)-L_2). A mixture of 4,4′-dibromo-1,1′-bi-2-naphthol (1.01 g, 2.25 mmol), pyridyl-4-boronic acid (0.69 g, 5.63 mmol), K_2CO_3 (1.56 g, 11.25 mmol), and $Pd(PPh_3)_4$ (0.26 g, 0.23 mmol) in toluene (75.0 mL), ethanol (50.0 mL) and H_2O (25.0 mL) was degassed and heated at reflux under N_2 for 72 hours. The solvent was removed under vacuum and the resulting red residue was washed with DCM (10.0 mL), the solid filtered and air dried to afford the product as a light brown powder (0.90 g, 91%). ^{1}H NMR (400 MHz, DMSO-d_6) δ 8.74 (d, 4H, J = 4.0 Hz), 7.74 (d, 2H, J = 8.0 Hz), 7.60 (m, 4H), 7.26 (s,

2H), 7.20 (m, 4H), 7.01 (m, 2H) ppm. $^{13}C\{^{1}H\}$ NMR (100 MHz, DMSO-d_6) δ 154.3, 150.0, 148.1, 137.7, 134.8, 131.7, 128.9, 128.1, 126.2, 125.5, 125.1, 123.0, 116.9 ppm. IR (ATR): 3520, 3406, 3056, 2695, 1607, 1587, 1420, 1370, 1333, 1199, 1065, 1008, 973, 830, 758, 612, 505, 445 cm^{-1}. ESI-MS (ESI^+, ACN) calc'd for $C_{30}H_{22}N_2O_2^{2+}$ $[M+2H]^{2+}$: 221.259, found: 221.084.

Computational Approach

Cluster model design and optimisation

We built four different cluster models to capture all possible interactions between the **1-OH** MOF's BINOL groups and the Moshers acid guests. The cluster models were built starting from the optimised unit cell of the MOF. The unit cell was optimised with periodic boundary conditions using the Vienna Ab Initio Simulation Program (VASP) [2-4]. For this optimisation, we used the PBE exchange-correlation functional[5] with Grimme's D3 dispersion correction, projector-augmented-wave (PAW) potentials available in VASP,[6] and a plane-wave basis with 600 eV kinetic energy cutoff. We used a Gamma Centred 2 × 2 × 2 k-point mesh to sample the Brillouin zone.

Each cluster model includes the middle **(*S*)-L2** ligand (shown in grey in Figure S1) and one of the four **(*S*)-L2** ligands surrounding the central middle ligand (each group is shown in a different colour in Figure S1). In the bulk structure, the **(*S*)-L2** groups are bound directly to the Zn atoms and the coordination environment around each Zn consists of one **(*S*)-L2** ligand and four D-Cam ligands. Interactions with the D-Cam ligand was not modelled as there are no accessible functional groups that would be able to bind effectively with either Moshers acid isomer. As a result, in the cluster models, the N atoms of each **(*S*)-L2** ligand were frozen to maintain the rigidity of the structure induced by the periodic framework environment. In addition, the aromatic hydrogens were also frozen to prevent the aromatic rings from rotating relative to each other, which would not be possible in the periodic structure. The frozen atoms were excluded from the frequency calculations to avoid the arise of spurious imaginary frequencies. Figure S1 shows that this overall approach leads to good overlap between the cluster models and the periodic structure thus providing validation for these models.

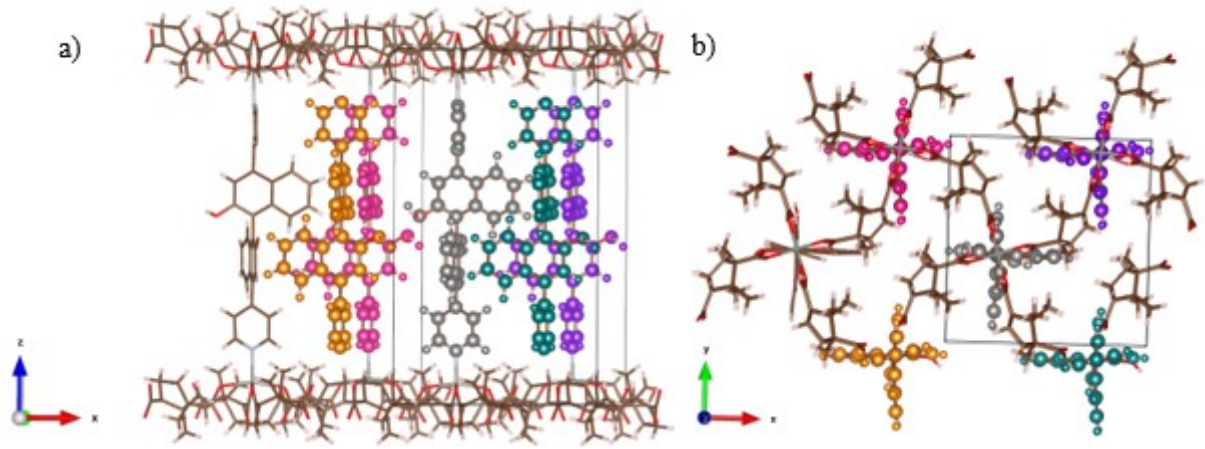

Figure S1. (a) Side view and (b) top view of the optimised structures of the cluster models used in this study to simulate the **1-OH** MOF overlayed with the MOF periodic structure. The **1-OH** crystal structure is shown with sticks only with teal representing carbon atoms, white representing hydrogen atoms, red representing oxygen atoms, dark blue representing nitrogen atoms and pink representing zinc atoms. Representation of bonds are omitted for clarity from the cluster models. Orange represents cluster model 1, pink represents cluster model 2, purple represents cluster model 3, dark green represents cluster model 4 and gray represents the middle ligand that is included in all four cluster models.

Optimisation of Moshers acid guests interacting with the 1-OH MOF

Starting guesses for the optimisations of the host-guest interaction geometries were built by focusing first on the R isomer of the Moshers acid guest. Starting structures prioritised either the formation of hydrogen bonds between the alcohol groups on both the guest (as part of the carboxylic acid group) and **1-OH** (cluster models 1 and 2) or the formation of π-π stacking interactions between the guest and the BINOL group on **1-OH** (cluster models 3 and 4). For each of the four cluster models, after the lowest energy optimised structures of the R isomer was found, a geometry optimisation for the S isomer was run with a starting guess based on the optimised geometry of the R isomer. This allows for a fair comparison between the two guests and their interaction with the MOF. Upon optimization, all structures were overlapped on the periodic **1-OH** structure to ascertain that optimised guest structures in the cluster model are reasonable given the confines of a periodic structure.

Gibbs free energy calculations

Gibbs free energies for all structures were calculated as so:

$$G = E_{gas}^{M2} + (G - E)_{gas}^{M1} + (E_{solv}^{M2} + E_{gas}^{M2}) \quad \text{Eq.S1}$$

where E indicates electronic energy, G indicates free energy with thermochemical corrections, the superscript M1 refers to energies obtained with the PBE+D3BJ/def2-SVP basis set, the superscript M2 refers to the refined energies with the ωB97x-D3BJ/def2-TZVP method, the subscript gas refers to gas phase energies and the subscript solv refers to the solution phase energies. Thermal corrections for MOF structures did not include translational or rotational components as these components do not apply to the extended MOF structure.

These energies were then used to calculate solvation corrections to the total free energy of each species as shown in Eq. 1.

Table S1. Crystallographic parameters for ligand *rac*-$\mathbf{L_1}$ and framework **1-OEt**.

	***rac*-$\mathbf{L_1}$**	**[Zn((*S*)-$\mathbf{L_1}$)(D-cam)$_2$]·4.9DMF·2.8H$_2$O (1-OEt)**
Empirical Formula	$C_{34}H_{28}N_2O_2$	$C_{26}H_{20}NO_5Zn$
M/g mol^{-1}	496.58	491.80
Temperature (K)	100(2)	100(2)
Crystal system	Triclinic	Orthorhombic
Space Group	*P*-1	$P2_12_12$
Crystal size (mm^3)	0.12 × 0.08 × 0.02	0.357 × 0.319 × 0.077
Crystal Colour	Yellow	Yellow
Crystal Habit	Block	Plates
a (Å)	9.5595(2)	13.11130(10)
b (Å)	9.8314(2)	13.42280(10)
c (Å)	14.8304(3)	22.5464(2)
α (°)	91.417(2)	90
β (°)	97.094(2)	90
γ (°)	110.267(2)	90
V (Å^3)	1294.09(5)	3967.95(6)
Z	2	2
ρ_{calc} (mg/mm^3)	1.274	0.823
Reflections collected	40441/5350 [R_{merge} = 0.0430]	65687/8420 [R_{merge} = 0.0508]
Data/parameters	5350/356	8420/323
Final R indexes [all data]	R_1 = 0.0506, wR_2 = 0.1297	R_1 = 0.0582, wR_2 = 0.1693
Goodness-of-fit on F^2	1.051	1.071
Largest diff. peak/hole (e$^-$ Å^{-3})	0.23/–0.29	1.29/–0.52
Flack parameter	N/A	0.145(15)

Table S2. Analysis of the possible coordination geometries using the SHAPE program for the 5-coordinate Zn(II) centres in **1-OEt**.

Geometry	Symmetry	1-OEt (Zn1)	1-OEt (Zn2)
PP-5	D_{5h}	32.479	32.677
vOC-5	C_{4v}	0.736	0.796
TBPY-5	D_{3h}	5.361	5.179
SPY-5	C_{4v}	**0.236**	**0.206**
JTBPY-5	D_{3h}	7.577	7.474

PP-5 = Pentagon; vOC-5 = Vacant octahedron (Johnson square pyramid, J1); TBPY-5 = Trigonal bipyramid; SPY-5 = Square pyramid; JTBPY-5 = Johnson trigonal bipyramid (J12). The minima values are indicated in bold.

Table S3. Values obtained through using the "Pore Analyser" function in Mercury 2023.1.0.

Parameter	Value
System Volume	3967.949 AÅ³
System Mass	1997.125 g/mol
System Density	0.835 g/cm Å³
Total surface area	379.92 AÅ²
Total surface area per volume	957.48 mÅ²/cm Å³
Total surface area per mass	1147.35 mÅ²/g
Network-accessible geometric volume	2269.335 AÅ³
Pore limiting diameter	4.15 Å
Maximum limiting diameter	7.25 Å

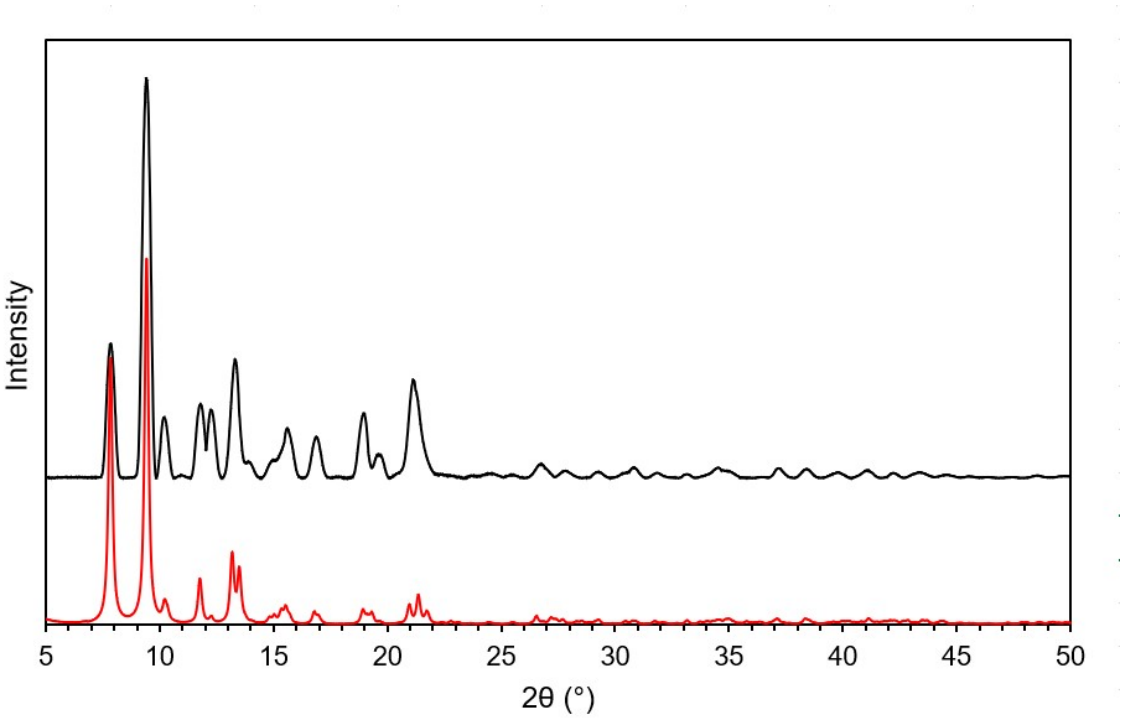

Figure S2. PXRD of **1-OEt** with calculated (red) and experimental (black) patterns.

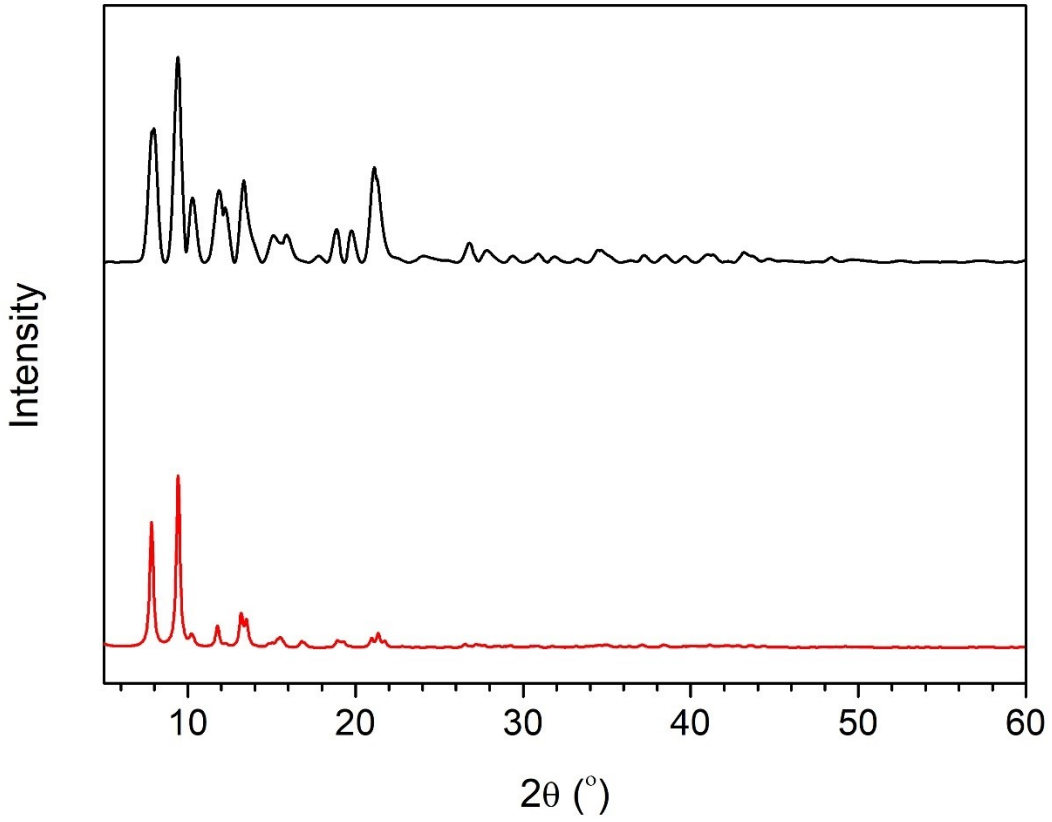

Figure S3. PXRD of **1-OH** plotted (red) against the calculated pattern for **1-OEt** (black).

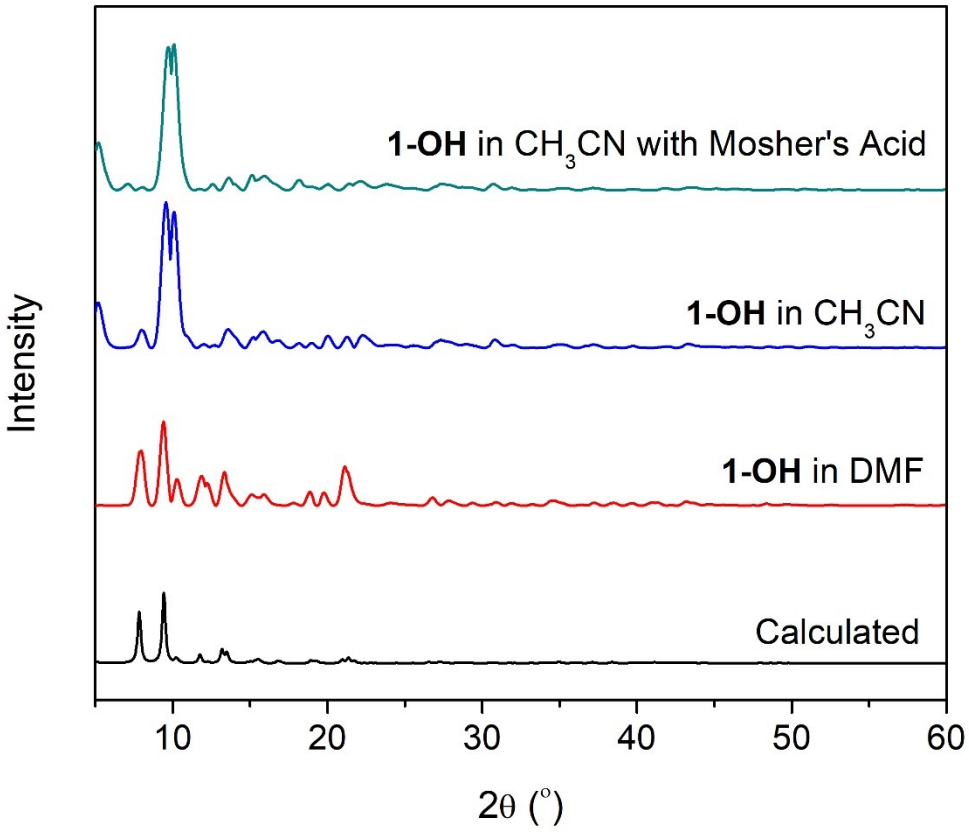

Figure S4. PXRD of **1-OH** plotted (red) against the calculated pattern for **1-OEt** (black).

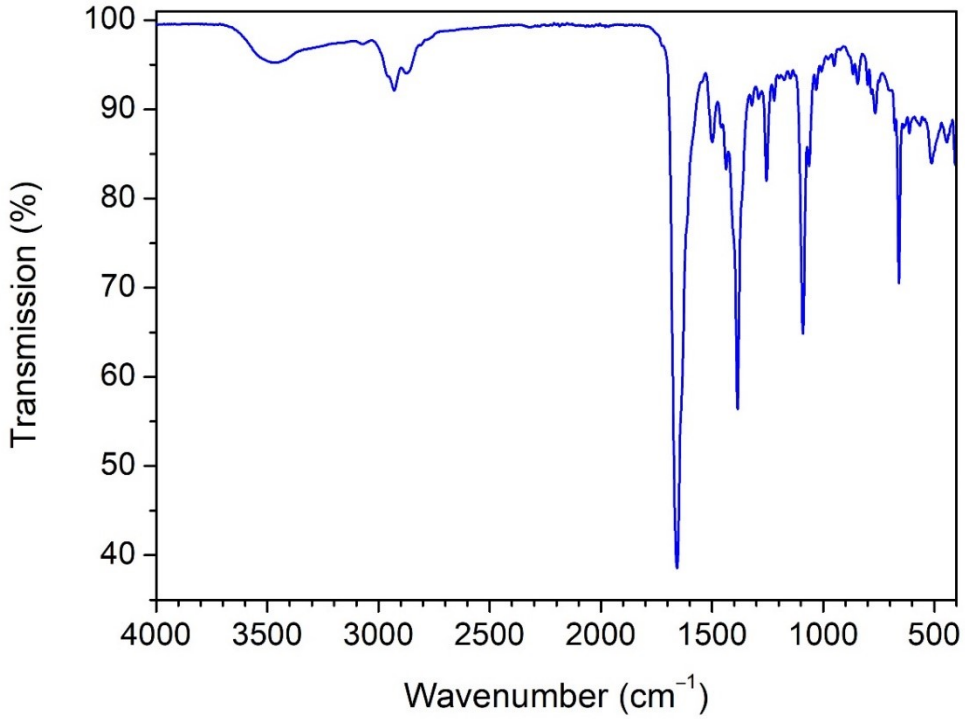

Figure S5. ATR-IR spectrum of **1-OEt**.

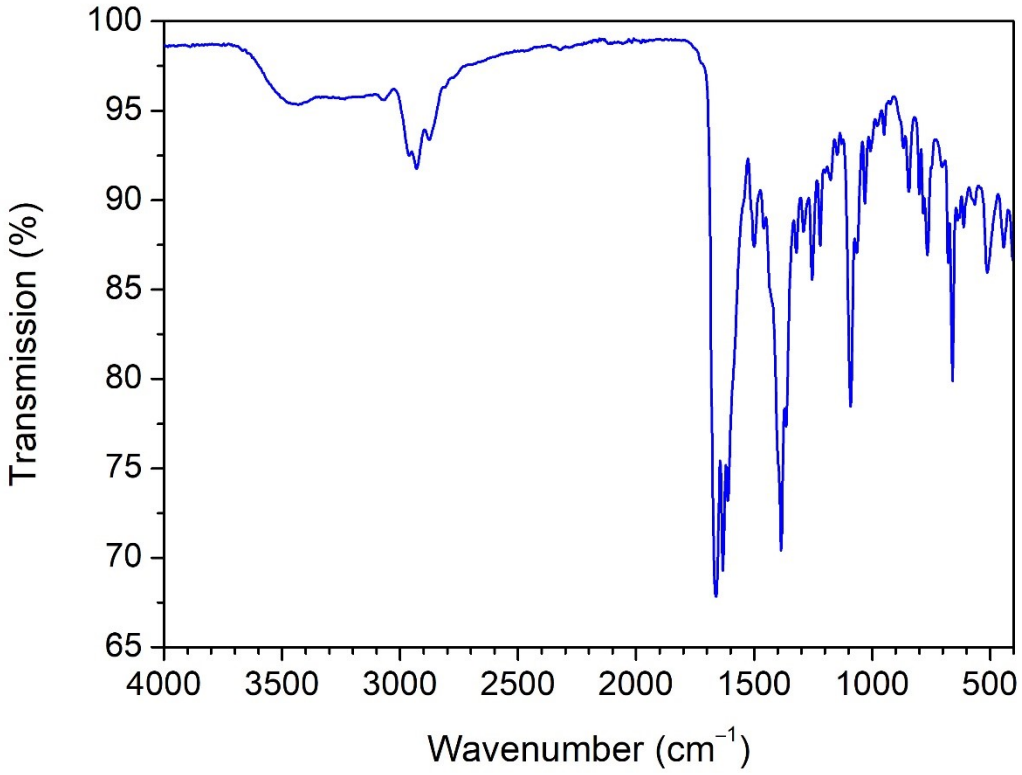

Figure S6. ATR-IR spectrum of **1-OH**.

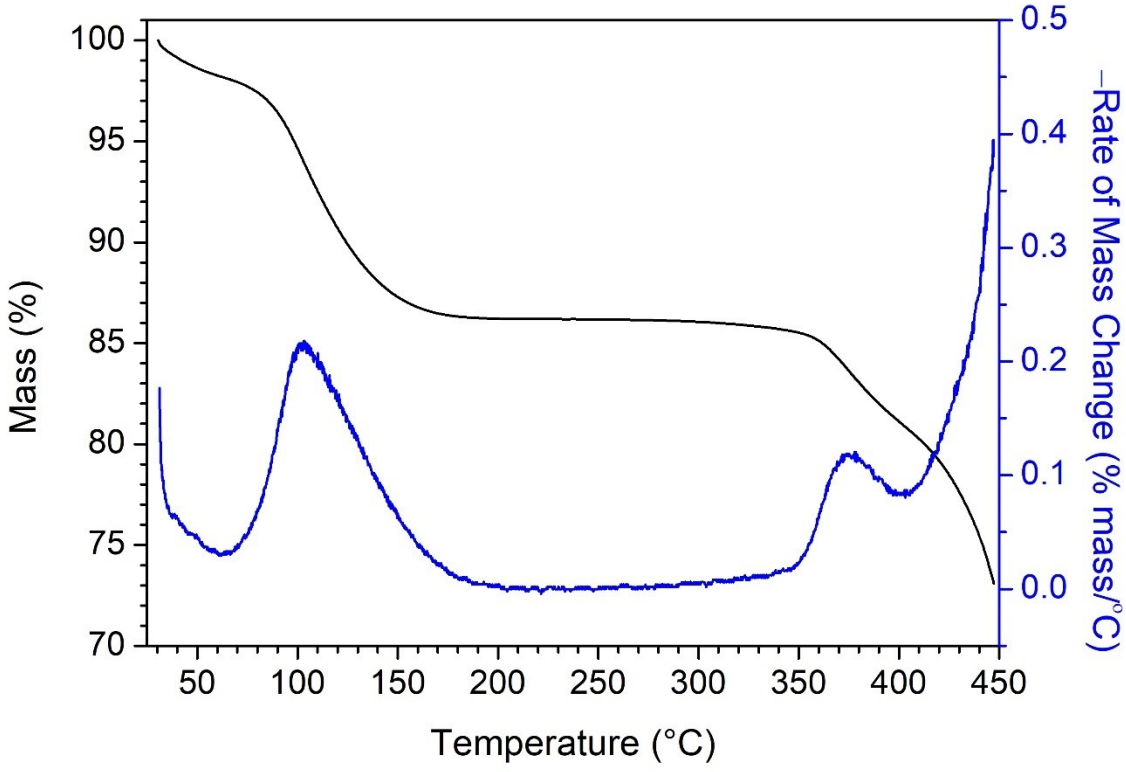

Figure S7. Thermal Gravimetric Analysis (TGA) of **1-OEt**.

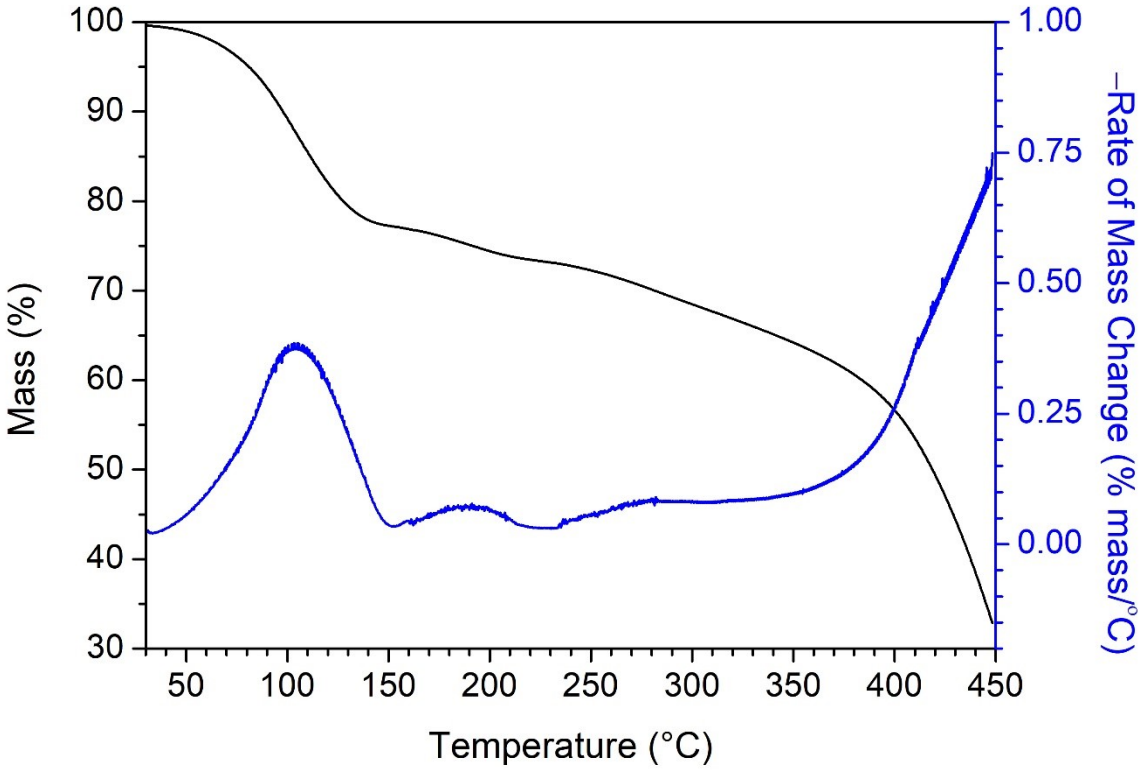

Figure S8. Thermal Gravimetric Analysis (TGA) of **1-OH**.

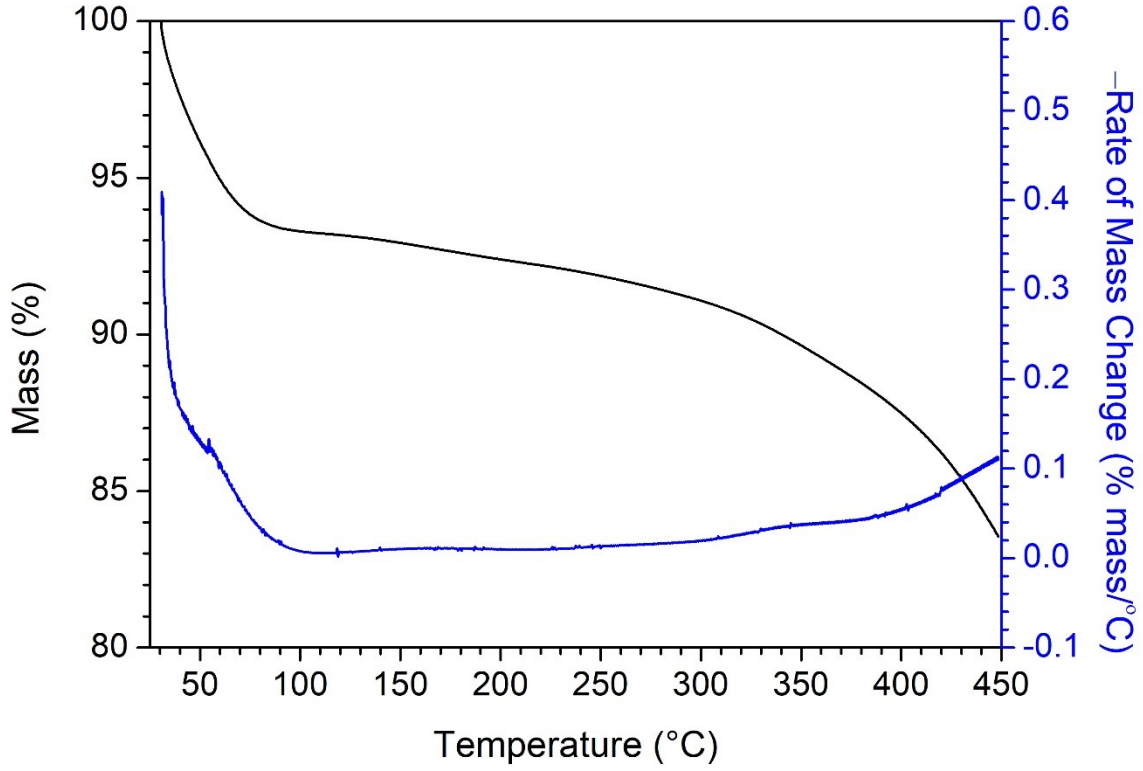

Figure S9. Thermal Gravimetric Analysis (TGA) of **1-OH** after solvent exchange with CH_3CN.

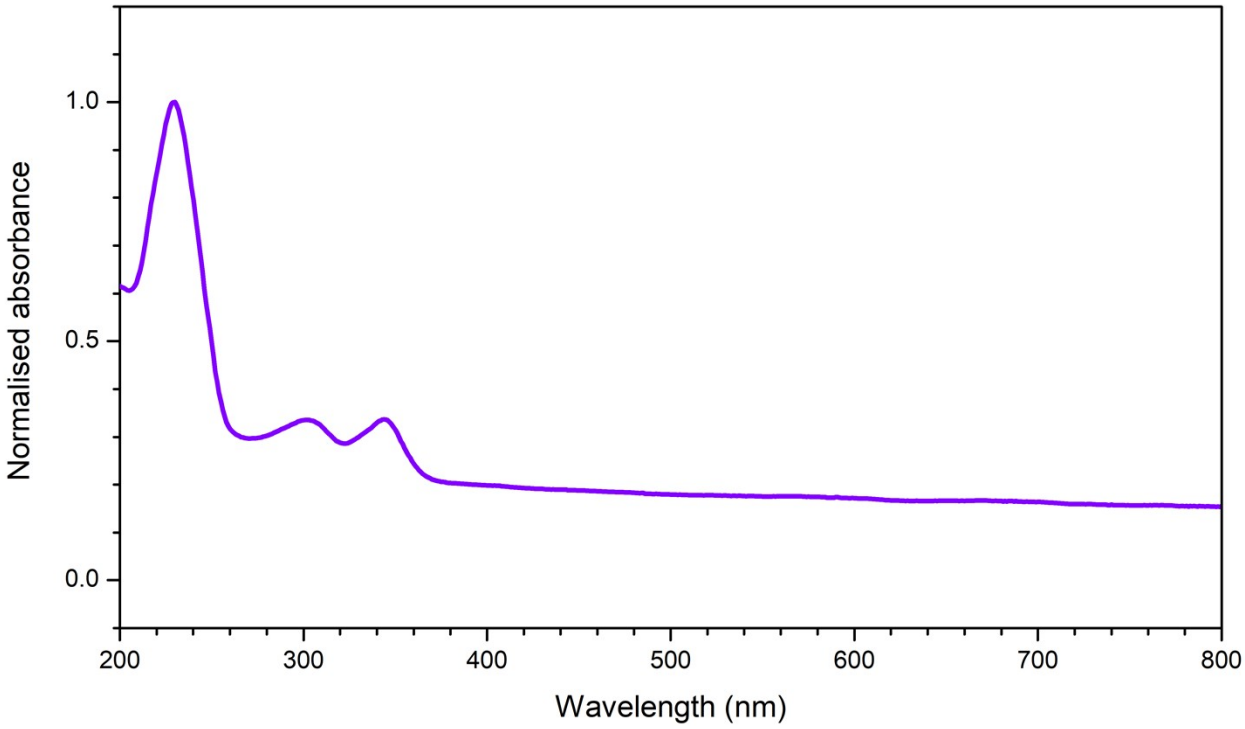

Figure S10. Absorption spectrum of **1-OH** in acetonitrile (10 μM).

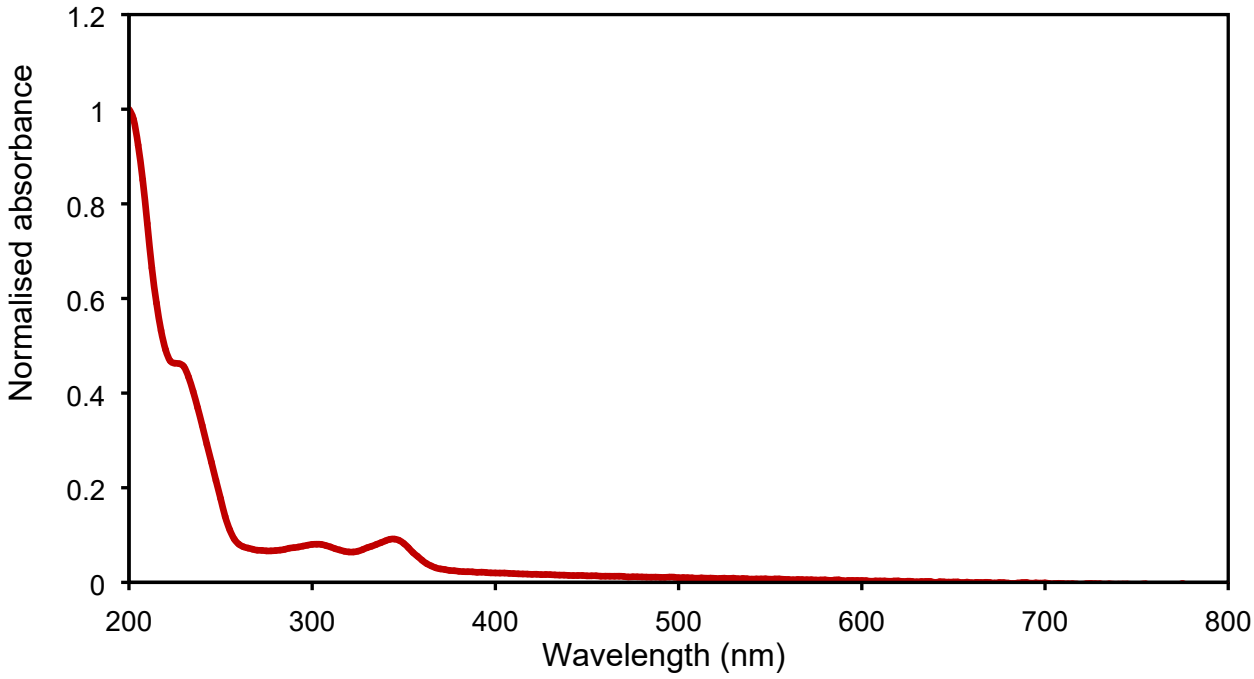

Figure S11. Absorption spectrum of **1-OEt** in acetonitrile (10 μM).

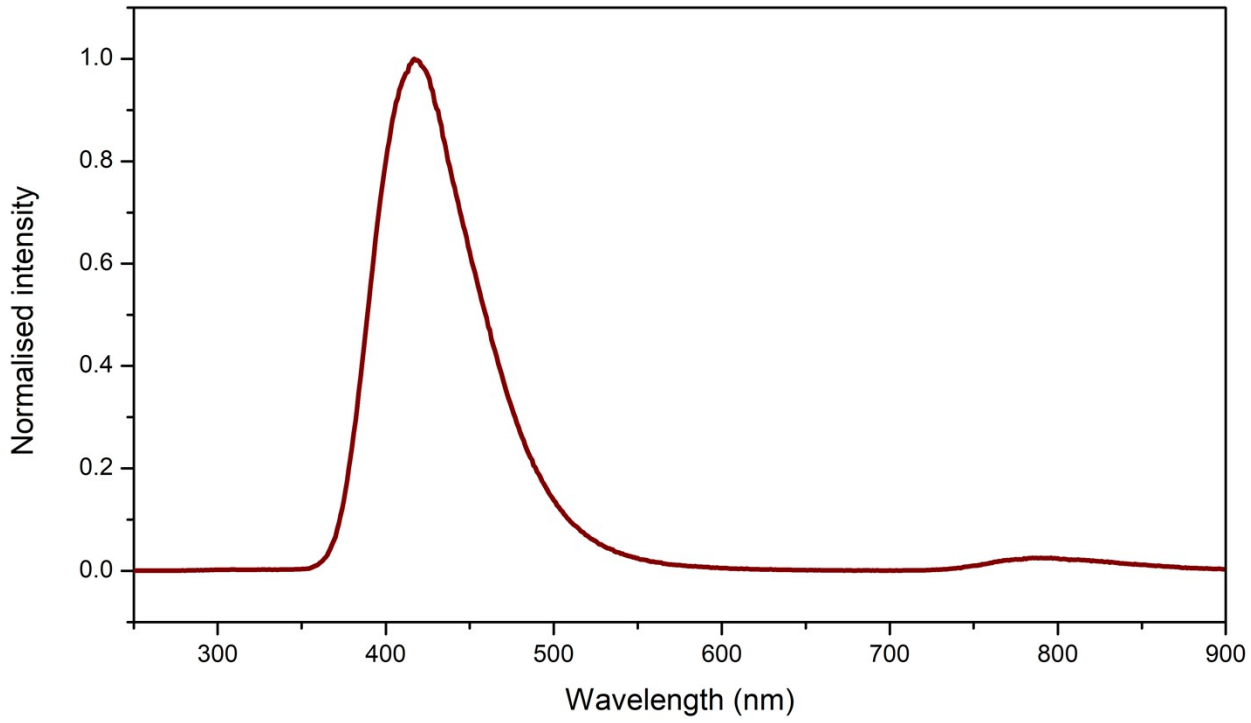

Figure S12. Emission spectrum of **1-OH** in acetonitrile (λ_{ex} = 229 nm).

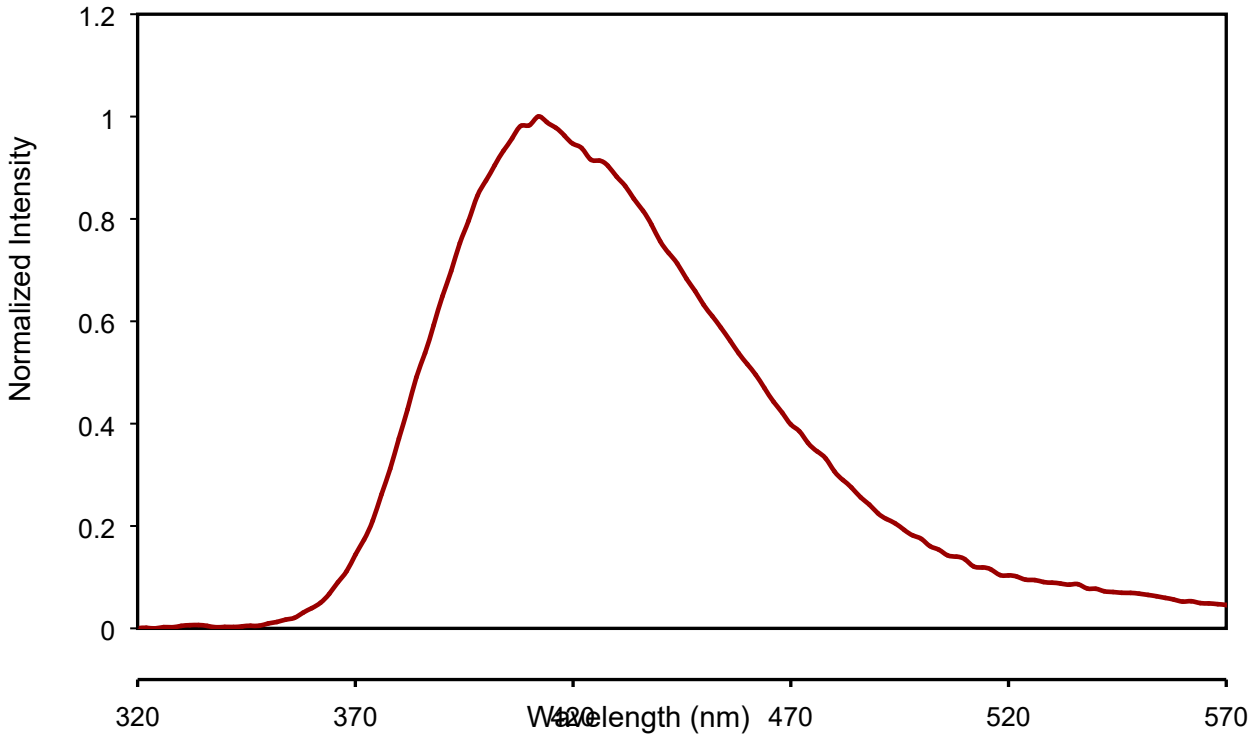

Figure S13. Emission spectrum of **1-OH** in acetonitrile (λ_{ex} = 302 nm).

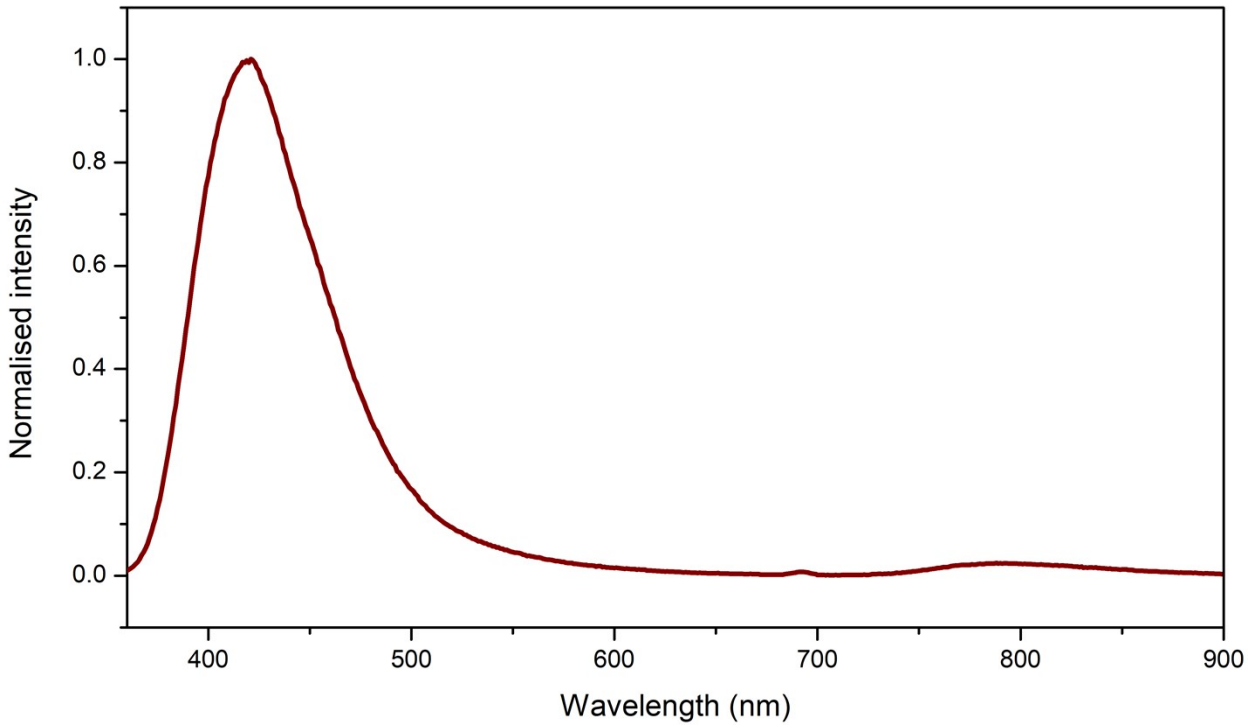

Figure S14. Emission spectrum of **1-OH** in acetonitrile (λ_{ex} = 344 nm).

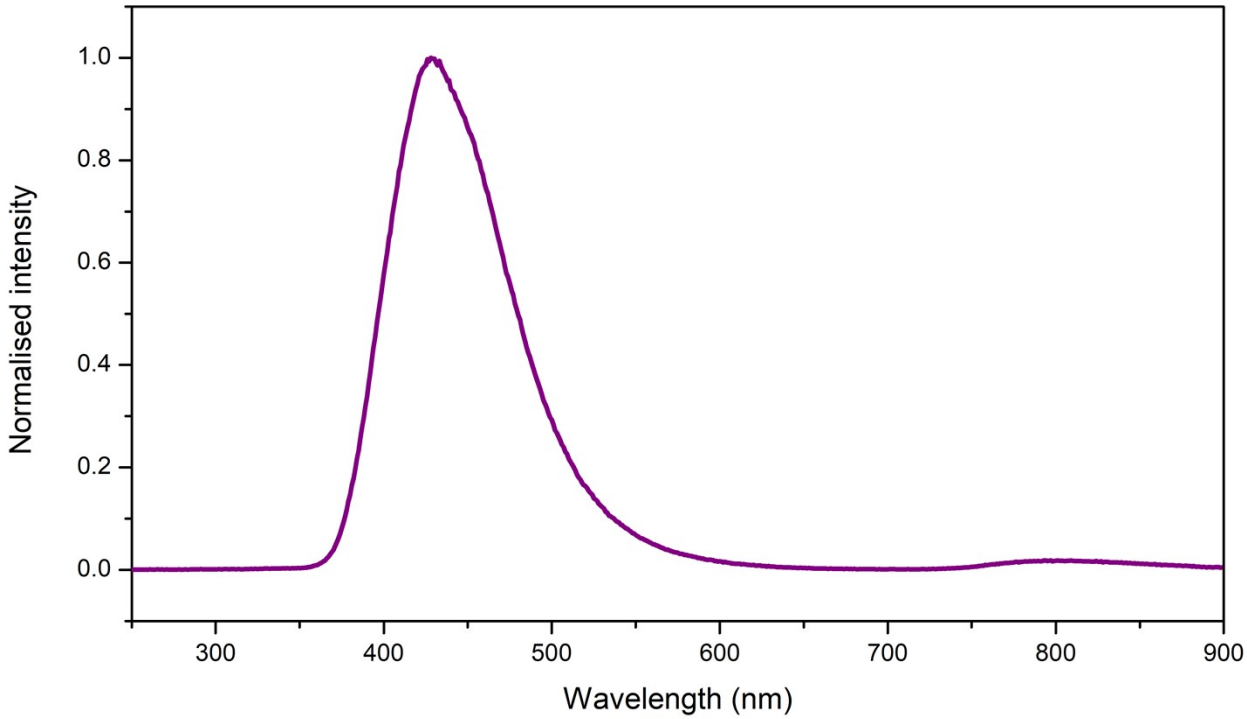

Figure S15. Emission spectrum of **1-OEt** in acetonitrile (λ_{ex} = 229 nm).

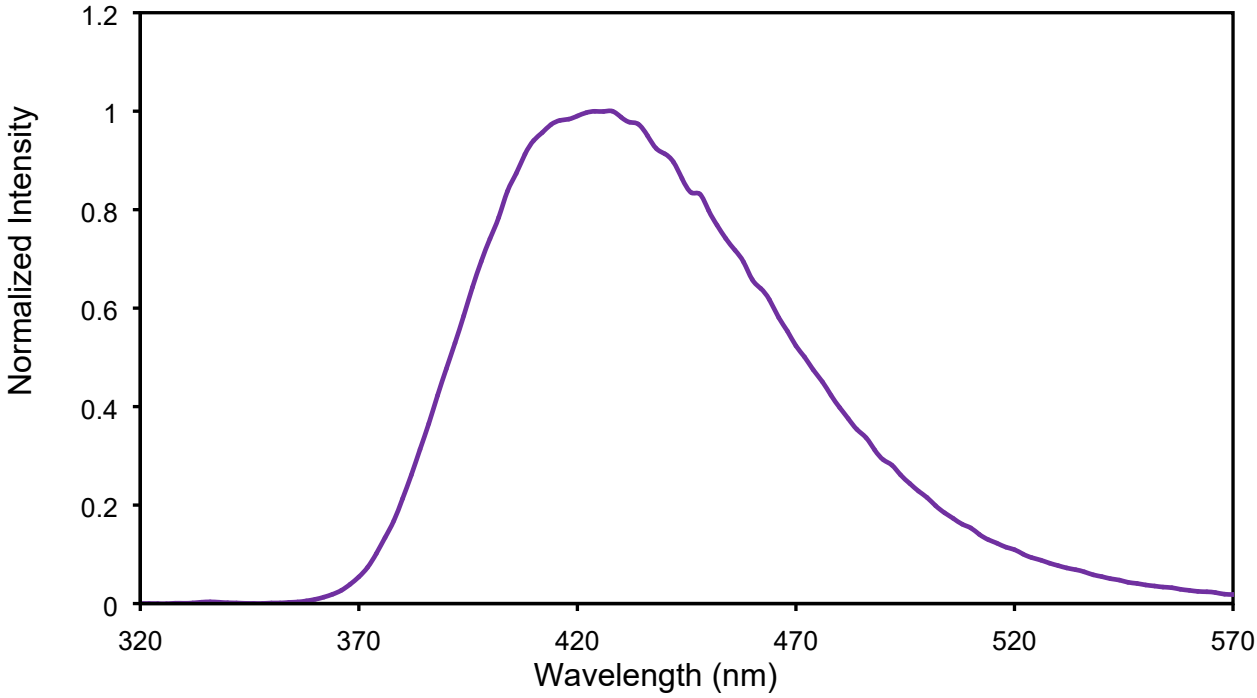

Figure S16. Emission spectrum of **1-OEt** in acetonitrile (λ_{ex} = 305 nm).

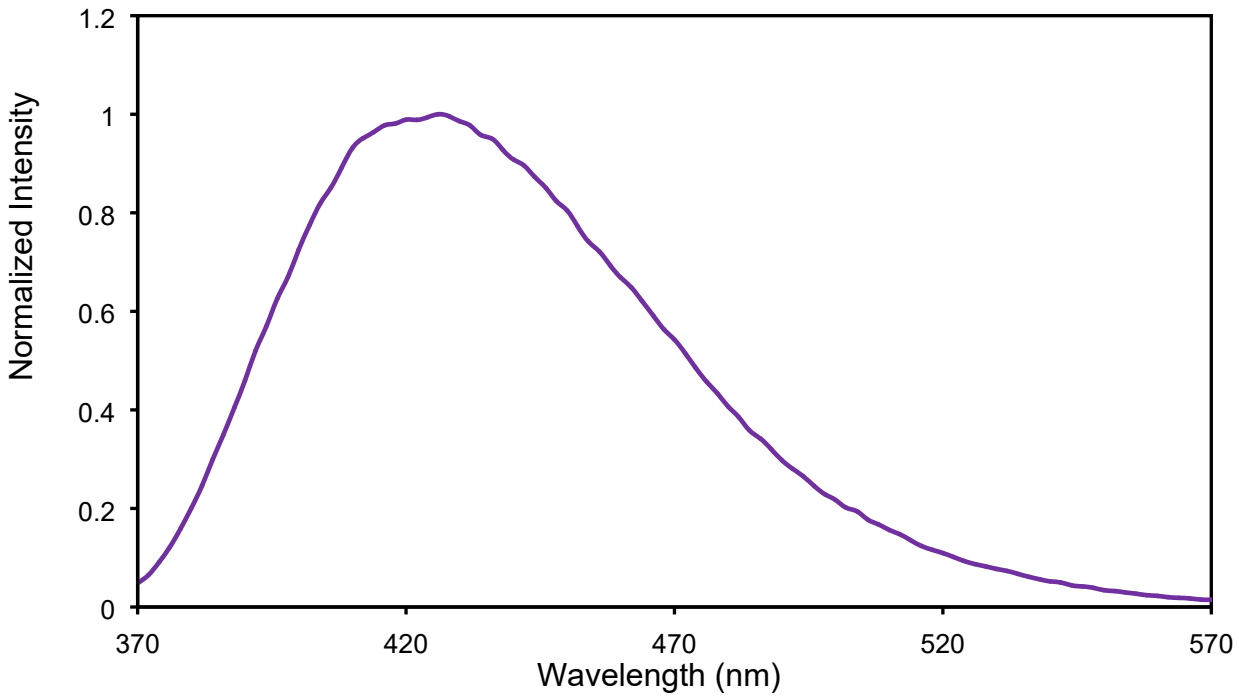

Figure S17. Emission spectrum of **1-OEt** in acetonitrile (λ_{ex} = 349 nm).

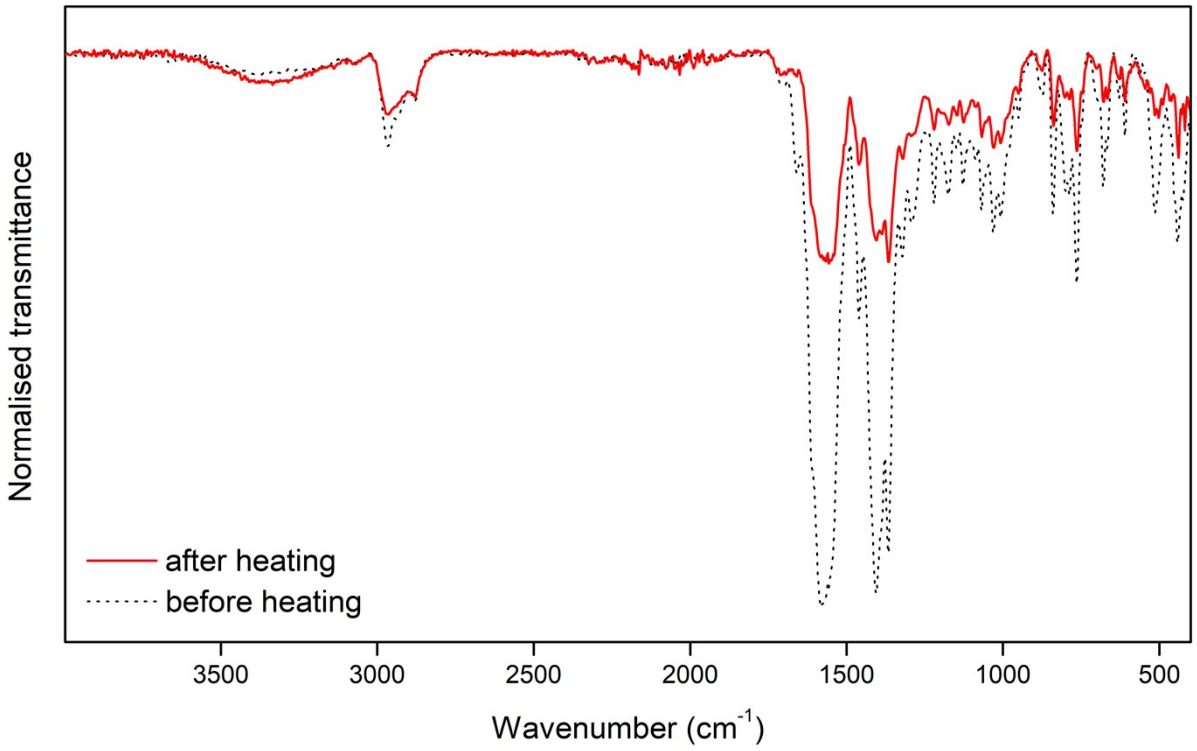

Figure S18. ATR-IR spectrum of **1-OH** heated for the removal of residual DMF.

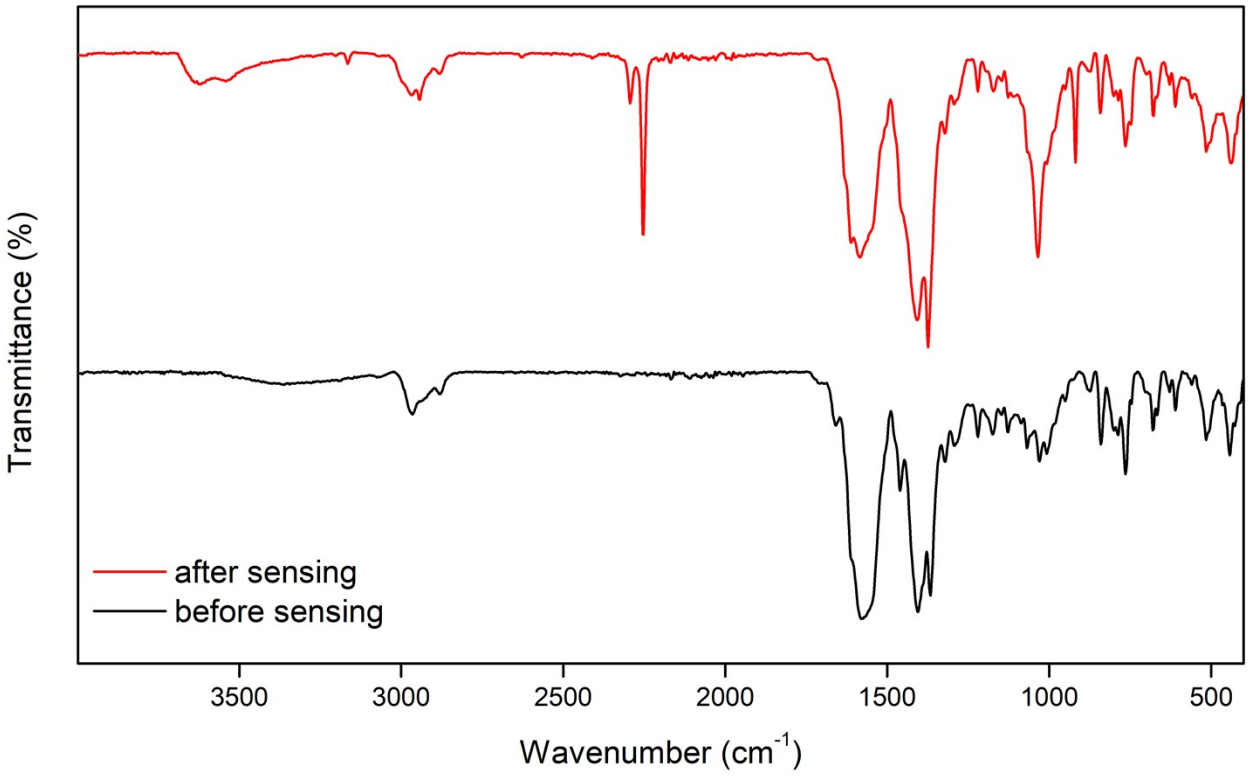

Figure S19. ATR-IR spectrum of **1-OH** before and after the fluorescence sensing experiment with Mosher's acid**.**

Table S4. Globally fit fluorescence decay parameters of the fluorophore with different (*R*)-Mosher's acid concentrations. Fitted, linked lifetimes (τ_1, τ_2) and weightings (α_i).

[(*R*)-Mosher's Acid] (mM)	α_1	τ_1 (ns)	α_2	τ_2 (ns)
0	0.12	0.83	0.88	2.26
0.08	0.17	0.83	0.83	2.26
0.16	0.23	0.83	0.77	2.26
0.32	0.26	0.83	0.74	2.26
0.48	0.29	0.83	0.71	2.26
0.64	0.33	0.83	0.67	2.26
0.80	0.32	0.83	0.68	2.26
0.87	0.33	0.83	0.67	2.26
0.95	0.37	0.83	0.63	2.26
1.11	0.37	0.83	0.63	2.26
1.19	0.39	0.83	0.61	2.26

Table S5. Globally fit fluorescence decay parameters of the fluorophore with different (*S*)-Mosher's Acid concentrations. Fitted, linked lifetimes (τ_1, τ_2) and weightings (α_i).

[(*S*)-Mosher's Acid] (mM)	α_1	τ_1 (ns)	α_2	τ_2 (ns)
0	0.29	1.21	0.71	2.31
0.08	0.34	1.21	0.66	2.31
0.16	0.43	1.21	0.57	2.31
0.32	0.49	1.21	0.51	2.31
0.48	0.52	1.21	0.48	2.31
0.64	0.55	1.21	0.45	2.31
0.80	0.57	1.21	0.43	2.31
0.87	0.58	1.21	0.42	2.31
0.95	0.58	1.21	0.42	2.31
1.11	0.57	1.21	0.43	2.31
1.19	0.58	1.21	0.42	2.31

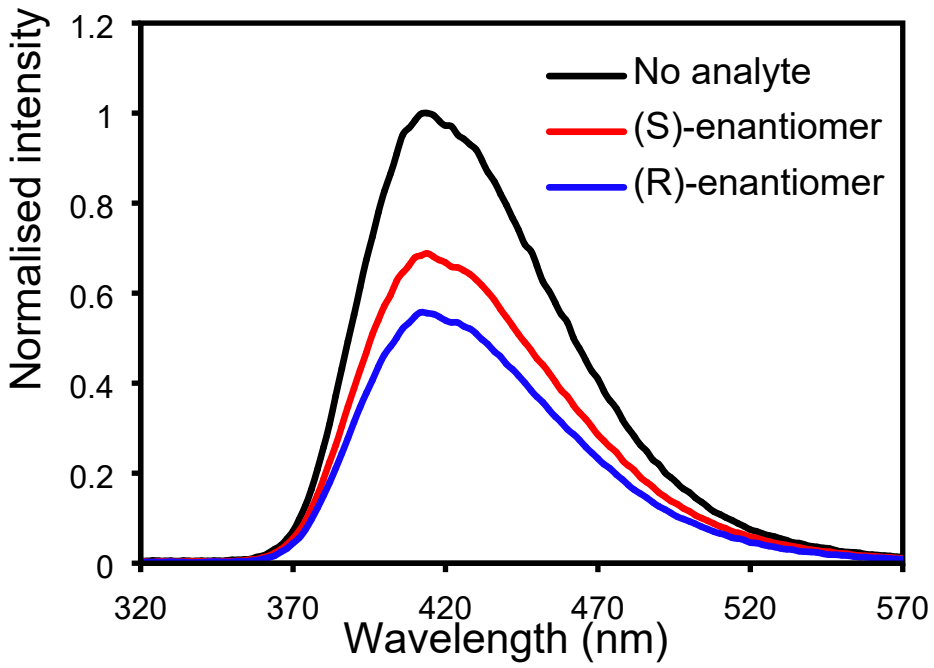

Figure S20. Fluorescence-based sensing experiment with Mosher's acid with **(*rac*)-1-OH** (λ_{ex} = 229 nm).

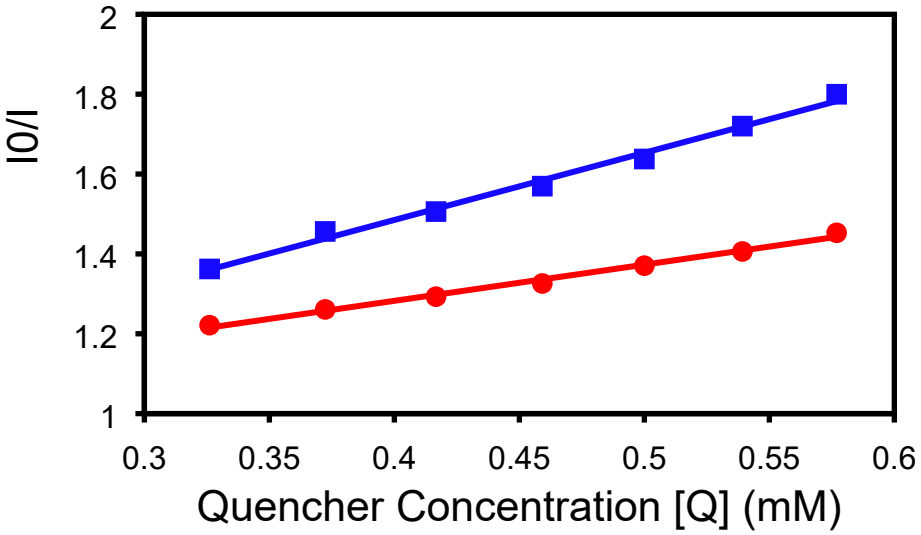

Figure S21. Stern-Volmer plots following the quenching of **(*rac*)-1-OH** by the enantiomers of Mosher's acid.

Additional computational results

Interactions of other cluster models with Mosher's acid

For all cluster models, we observe H-F interactions between the aromatic hydrogens and the fluorine atoms on the Mosher's acid guests.

For cluster model 1, as discussed in main text, the R isomer has no significant binding interactions with **1-OH** apart from H-F interactions whilst the S isomer can form a hydrogen bond between its carboxylic acid group and the alcohol group of the BINOL ligand. This hydrogen bond formed for the S isomer with **1-OH** leads to a stronger MOF-guest interaction relative to the R isomer.

For cluster model 2 (Figure **S22**), there are alcohol groups present in this pore cavity that may allow Mosher's acid to bind preferably to 1-OH. We find that the R isomer has a hydrogen bonding interaction between its carboxylic acid group and the alcohol group of the BINOL ligand (hydrogen bond length = 2.0 Å), whilst the S isomer has no additional significant binding interactions with **1-OH** apart from H-F interactions. Although the R isomer has hydrogen bonding interactions, there are no additional electrostatic interactions from the aromatic ring. As a result, there is an unfavourable exchange free energy of the guest with the acetonitrile solvent.

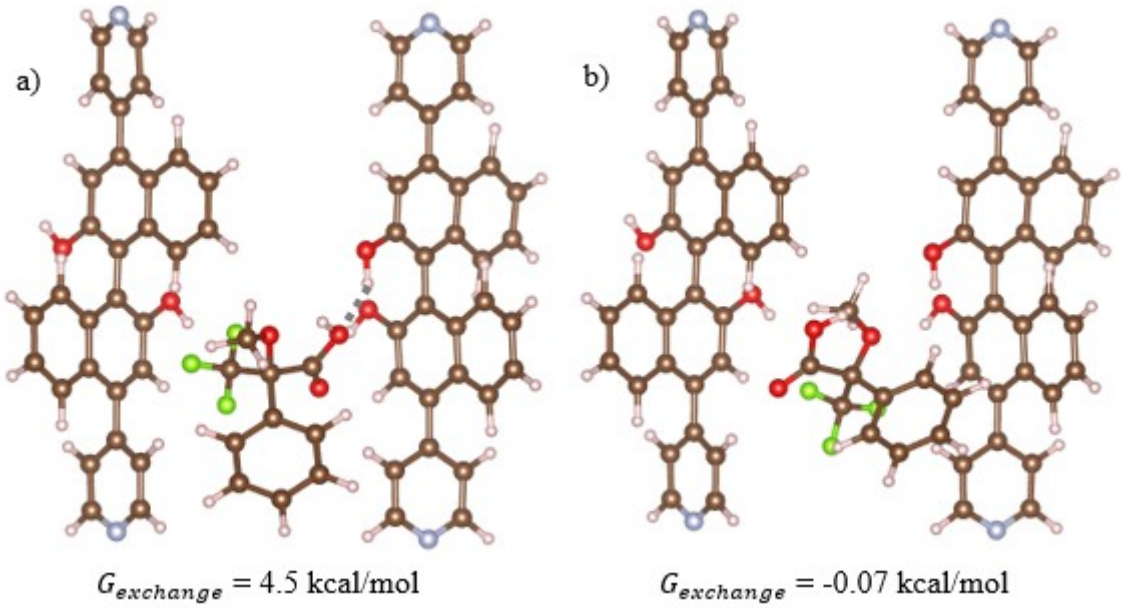

Figure S22. Optimised geometries for the most stable cluster model 2 structures representing **1-OH** and the a) R and b) S isomers of Moshers acid. In this structure, **1-OH** is represented using

cluster model 2 which is vertically aligned with the z axis relative to the periodic structure (refer to Figure S1). $G_{exchange}$ refers to the exchange free energy of the guest with the acetonitrile solvent. Hydrogen bonds shown in dotted grey, grey represents carbon atoms, white represents hydrogen atoms, red represents oxygen atoms, teal representing nitrogen and green represents fluorine atoms.

For cluster model 3 (Figure S23), there is one alcohol group present in this pore cavity alongside aromatic rings that provide potential sites for π-π stacking interactions that may allow Mosher's acid to bind to **1-OH**. We find that the R isomer shows weak hydrogen bonding interactions between its carboxylic acid group and the pyridine rings of **1-OH** (hydrogen bond length = 2.5 Å), while the S isomer does not show any additional binding interactions apart from the H-F interactions.

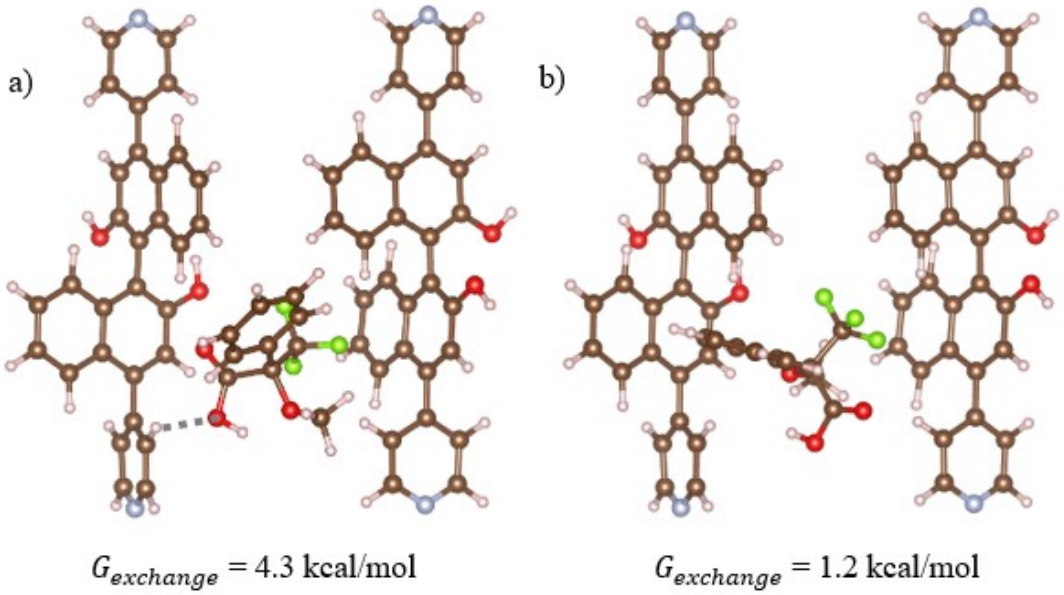

Figure S23. Optimised geometries for the most stable cluster model 3 structures representing **1-OH** and the a) R and b) S isomers of Moshers acid. In this structure, **1-OH** is represented using cluster model 3 which is vertically aligned with the z axis relative to the periodic structure (refer to Figure S1). $G_{exchange}$ refers to the exchange free energy of the guest with the acetonitrile solvent. Hydrogen bonds shown in dotted grey, grey represents carbon atoms, white represents hydrogen atoms, red represents oxygen atoms, teal representing nitrogen and green represents fluorine atoms.

For cluster model 4 (Figure S24), the same potential interactions are present as in cluster model 3 that may allow binding of Moshers acid to **1-OH**. We find that for both the R and S isomers, there are weak hydrogen bonding interactions between their carboxylic acid group and the aromatic hydrogen of the BINOL ligand (hydrogen bond length = 2.6, 2.5 Å respectively), with weak π-π stacking interactions in both structures (π-π distance = 4.3 Å). These structures are comparable to each other, suggesting that this pore cavity does not selectively bind to either isomer.

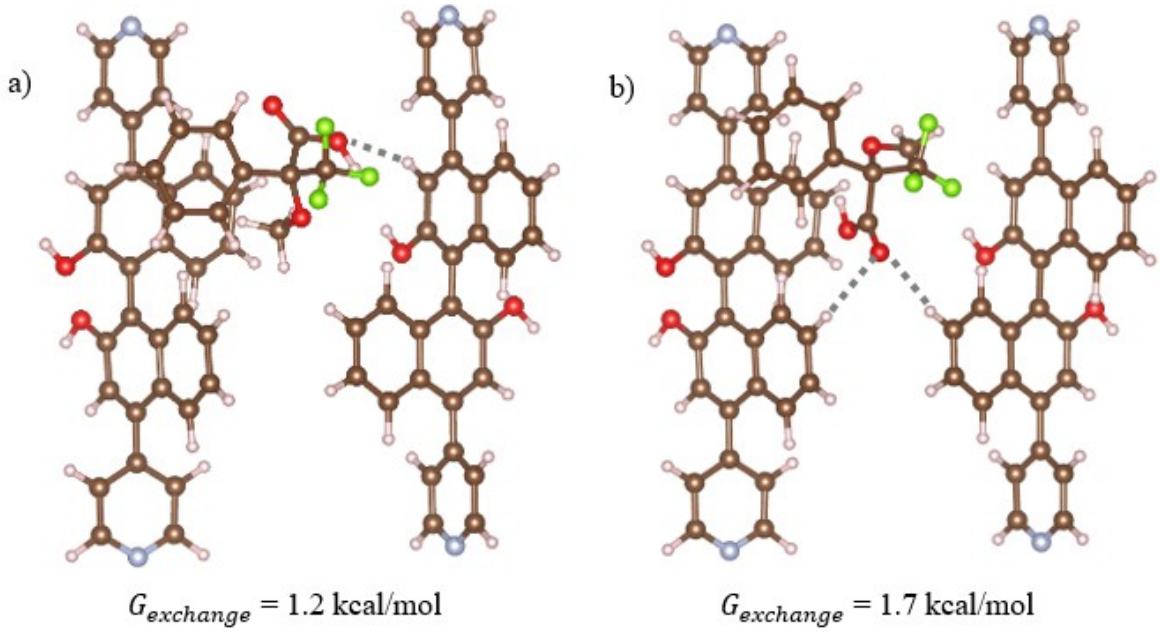

Figure S24. Optimised geometries for the most stable cluster model 4 structures representing **1-OH** and the a) R and b) S isomers of Moshers acid. In this structure, **1-OH** is represented using cluster model 4 which is vertically aligned with the z axis relative to the periodic structure (refer to Figure S1). $G_{exchange}$ refers to the exchange free energy of the guest with the acetonitrile solvent. Hydrogen bonds shown in dotted grey, grey represents carbon atoms, white represents hydrogen atoms, red represents oxygen atoms, teal representing nitrogen and green represents fluorine atoms.

References

1. Q.-W. Zhang, D. Li, X. Li, P. B. White, J. Mecinović, X. Ma, H. Ågren, R. J. M. Nolte and H. Tian, *J. Am. Chem. Soc.*, **2016**, *138*, 13541-13550.
2. G. Kresse and J. Hafner, *Phys. Rev. B*, **1993**, *47*, 558-561.
3. G. Kresse and J. Furthmüller, *Phys. Rev. B*, **1996**, *54*, 11169-11186.
4. G. Kresse and J. Furthmüller, *Comput. Mater. Sci.*, **1996**, *6*, 15-50.
5. J. P. Perdew, K. Burke and M. Ernzerhof, *Phys. Rev. Lett.*, **1996**, *77*, 3865-3868.
6. G. Kresse and D. Joubert, *Phys. Rev. B*, **1999**, *59*, 1758-1775.